Dependence of direct and rescattered photoelectron spectra of fluorine anions on orbital symmetry in a short laser pulse

Jian-Hong Chen [1,*] Xiang-Ru Xiao,[2] Song-Feng Zhao [3,†] and Liang-You Peng[2,4]

[1]*School of Electronic and Information Engineering, Lanzhou City University, Lanzhou 730070, China*

[2]*School of Physics and State Key Laboratory for Mesoscopic Physics, Peking University, Beijing 100871, China*

[3]*College of Physics and Electronic Engineering, Northwest Normal University, Key Laboratory of Atomic and Molecular Physics and Functional Materials of Gansu Province, Lanzhou 730070, China*

[4]*Frontiers Science Center for Nano-optoelectronics and Collaborative Innovation Center of Quantum Matter, Beijing 100871, China*

(Received 2 December 2019; accepted 21 February 2020; published 16 March 2020)

We theoretically investigate the photoelectron spectra of fluorine anions by a few-cycle linearly polarized laser pulse for different atomic orbitals, which are calculated by an exact solution to the time-dependent Schrödinger equation and by the strong-field approximation, respectively. Through the comparison of results by both methods, we show that the initial orbital symmetry strongly affects the main shape of the photoelectron spectra. Based on the saddle-point method, we find that the orbital symmetry only affects the intracycle interference for the low-energy electron spectra. More importantly, it is found that the elastic scattering differential cross section leaves different fingerprints in the photoelectron spectra for atomic orbitals with different magnetic quantum numbers.

DOI: 10.1103/PhysRevA.101.033409

I. INTRODUCTION

Strong-field ionization or detachment is the cornerstone for understanding numerous physical phenomena in attosecond sciences [1,2]. Much important information on the ionization process and target structure can be revealed from the angle-resolved photoelectron spectra of atoms and negative ions [3–12]. For example, the photoelectron energy spectra of above-threshold ionization (ATI), which is characterized by peaks separated by one photon energy, can be explained as the interference of photoelectron wave packets separated in time by one laser period, i.e., the so-called intercycle interferences [11,12]. The interferences of photoelectron wave packets arising within one laser period are called intracycle interference [11,12]. Once the effect of the long-range Coulomb potential has been excluded, intracycle interferences may give rise to the dominant interference fringes in low-energy photoelectron momentum spectra.

Most previous observations had been interpreted based on the assumption of valence s orbitals, although many atoms and negative ions carry valence p orbitals. Recently, the effect of atomic orbitals with different magnetic quantum numbers on the photoelectron spectra has been studied in various strong-field schemes [13–18], such as linearly [13], circularly [14,15], and elliptically [16] polarized laser pulses. However, for most strong-field ionization of neutral atoms, the long-range Coulomb potential is crucial in reproducing the correct photoelectron spectra [19,20]. In order to reduce the effect of the Coulomb potential, we propose the photoelectron spectra of fluorine anions with valence p orbitals as an ideal platform to identify the effect of orbital symmetry. The main advantage of studying strong-field detachment for fluorine anions is the short-range potential between the neutral core and the ejected electron. A series of experiments on the angle-resolved electron spectra for fluorine anions have been successfully conducted by Kiyan *et al.* [21–25]. The strong-field approximation (SFA) model ignoring the Coulomb potential after ionization is well established by the measurement of hydrogen anions and fluorine anions [21–29].

On the other hand, as is well known, the momentum spectra of a high-energy photoelectron encodes the structural information of the atom, negative ion, or molecule [30]. It has been theoretically predicted and experimentally confirmed that the elastic scattering differential cross section (DCS) can be extracted from momentum spectra of the rescattered photoelectrons [31–34]. However, in most work, the effect of initial orbital symmetry on the high-energy electron spectra and the extraction of elastic scattering DCS is rarely investigated. Recently, the effect of orbital symmetry has been considered in neutral atoms' single ionization driven by bicircular laser fields [35] or nonsequential double ionization driven by linearly polarized laser pulses [36]. As a more fundamental example, it is essential to revisit the effect of orbital symmetry on the rescattered electron spectra of fluorine anions, which is characterized by the short-range potential and valence p orbitals.

In this paper, based on the numerical calculations from the time-dependent Schrödinger equation (TDSE) and SFA model [3], we investigate the direct and rescattered photoelectron spectra of fluorine anions for different orbital symmetry by a few-cycle linearly polarized laser pulse. Our SFA calculations of electron spectra for fluorine anions, apart from the

*chenyuwen1982@163.com

†zhaosf@nwnu.edu.cn

high-energy electron spectra for magnetic quantum number $m = 0$, have shown good agreement with those obtained by the TDSE. For the low-energy electron spectra, we demonstrate that the orbital symmetry only affects the intracycle interference, but has limited influence on the intercycle interference, based on the saddle-point (SP) method. Moreover, we find that the elastic scattering DCS leaves different fingerprints in the photoelectron spectra for atomic orbitals with magnetic quantum numbers $m = 0$ or $m = 1$, respectively. Atomic units are used in this paper unless stated otherwise.

II. THEORETICAL METHODS

A. TDSE

We numerically solve the TDSE within the single active electron approximation. In the velocity gauge, the TDSE reads

$$i\frac{\partial}{\partial t}\psi(\boldsymbol{r},t) = \left[-\frac{1}{2}\nabla^2 + V(r) + i\boldsymbol{A}(t)\cdot\nabla\right]\psi(\boldsymbol{r},t), \quad (1)$$

where $\boldsymbol{A}(t) = -\int \boldsymbol{E}(t')dt'$ is the vector potential of the laser pulse. The electric field of a linearly polarized laser pulse (along the z axis) can be written as

$$\boldsymbol{E}(t) = E_0\cos^2\left(\frac{\pi t}{\tau}\right)\cos(\omega t + \delta)\hat{z}, \quad (2)$$

in the time interval $(-\tau/2, \tau/2)$ and zero elsewhere. In Eq. (2), E_0 is the peak electric field of the laser pulse with frequency ω. τ is the total pulse duration and δ is its carrier-envelope phase (CEP). In our calculations, we use a three-cycle laser pulse with a peak intensity of $1.7 \times 10^{13}\,\mathrm{W/cm^2}$ at the wavelength of 1400 nm. Since we do not discuss the CEP effect, δ is thus set as zero in this work.

For fluorine anions, we use the double Yukawa potential as follows [37],

$$V(r) = -a_1\frac{e^{-a_2 r}}{r} - a_3\frac{e^{-a_4 r}}{r}, \quad (3)$$

where $a_1 = 5.137$, $a_2 = 1.288$, $a_3 = 3.863$, and $a_4 = 3.545$ [21]. The above model potential can reproduce the ground-state energy of the fluorine anions, i.e., $I_p = 3.4\,\mathrm{eV}$. The details about the TDSE calculations can be found in previous work [5–7,38,39]. In the calculations presented below, the converged TDSE results are obtained by setting $r_{\max} = 3600$ a.u., the radial grid spacing $dr = 0.05$ a.u., the time step $dt = 0.05$ a.u., and the maximum number of partial waves $l_{\max} = 50$.

B. SFA model

Although the TDSE results can accurately produce the photoelectron spectra, the physical origins of interference patterns are hard to identify. In what follows, we briefly introduce the SFA model [3,40–42], which can give some insights. In the SFA model, the transition amplitude from an initial ground state $|\psi_{lm}\rangle$ into a final Volkov state $|\psi_{\boldsymbol{p}}\rangle$ with a momentum $\boldsymbol{p}$ is given by $M(\boldsymbol{p}) = M^{(1)}(\boldsymbol{p}) + M^{(2)}(\boldsymbol{p})$, in which $M^{(1)}(\boldsymbol{p})$ corresponds to the standard SFA model for calculating the direct photoelectron spectra (SFA1) and $M^{(2)}(\mathbf{p})$ for the high-energy electron spectrum (SFA2). They are, respectively, given by

$$M^{(1)}(\boldsymbol{p}) = -i\int_{-\infty}^{+\infty} dt_0\langle\psi_{\boldsymbol{p}}(t_0)|\boldsymbol{r}\cdot\boldsymbol{E}(t_0)|\psi_{lm}\rangle\exp(iI_p t_0), \quad (4)$$

$$M^{(2)}(\boldsymbol{p}) = -\int_{-\infty}^{+\infty} dt_1\int_{-\infty}^{t_1} dt_0\left[\frac{2\pi}{i(t_1-t_0)}\right]^{3/2} \times\langle\psi_{\boldsymbol{p}}(t_1)|V(\boldsymbol{r})|\boldsymbol{k}+\boldsymbol{A}(t_1)\rangle \times\langle\boldsymbol{k}+\boldsymbol{A}(t_0)|\boldsymbol{r}\cdot\boldsymbol{E}(t_0)|\psi_{lm}\rangle\exp\left[iS(\boldsymbol{k};t_1,t_0)\right], \quad (5)$$

in which the action in Eq. (5) is defined as

$$S(\boldsymbol{k};t_0,t_1) = -\int_{t_0}^{t_1} dt\left\{\frac{[\boldsymbol{k}+\boldsymbol{A}(t)]^2}{2} + I_p\right\} - \int_{t_1}^{\infty} dt\left\{\frac{[\boldsymbol{p}+\boldsymbol{A}(t)]^2}{2} + I_p\right\}, \quad (6)$$

with $\boldsymbol{k} = -\int_{t_0}^{t_1}\boldsymbol{A}(t)dt/(t_1-t_0)$ being the electron canonical momentum between the ionization time t_0 and the recollision time t_1. Physically, Eq. (5) can be understood with the three-step model: Firstly, the electron is ionized from the initial state $|\psi_{lm}\rangle$ at time t_0; secondly, it propagates with the momentum $\boldsymbol{k}$ from t_0 to t_1; finally the photoelectron is rescattered by the residual core into the final state $|\psi_{\boldsymbol{p}}\rangle$.

With the z axis taken as the quantization axis, the initial-state wave function for fluorine anions can be given by [43]

$$\psi_{1m}(\boldsymbol{r}) = \frac{B}{r}\exp(-\kappa r)Y_{1m}(\hat{r}), \quad (7)$$

where $B = 0.75$ and $\kappa = \sqrt{2I_p}$. The direct electron amplitude of Eq. (4) can be calculated using the SP method as follows [43]:

$$M^{(1)}(\boldsymbol{p}) = -(2\pi)^{3/2}B\sum_{t_s} Y_{1m}(\hat{q}_s)\frac{\exp(if(t_s))}{\sqrt{-if''(t_s)}}, \quad (8)$$

where $f(t_s) = -\int_{t_s}^{\infty}([\boldsymbol{p}+\boldsymbol{A}(t')]^2/2 + I_p)dt'$ and $f''(t_s) = 2\boldsymbol{E}(t_s)\cdot[\boldsymbol{p}+\boldsymbol{A}(t_s)]$. In Eq. (8), t_s is the complex root of the SP equation $[\boldsymbol{p}+\boldsymbol{A}(t_s)]^2 + 2I_p = 0$ and $\hat{q}_s$ is the unit vector of the complex canonical momentum $\boldsymbol{p}+\boldsymbol{A}(t_s)$. Without loss of generality, we choose $\boldsymbol{p}+\boldsymbol{A}(t_s) = i\kappa$ in the following derivations. For the atomic orbitals $m = 0$ and $m = \pm 1$, it is easy to show the transition probability amplitudes,

$$M_0^{(1)}(\boldsymbol{p}) = -\sqrt{6}\pi B\sum_{t_s}\frac{A(t_s)+p_\parallel}{i\kappa}\frac{\exp[if(t_s)]}{\sqrt{-if''(t_s)}}, \quad (9)$$

$$M_{\pm 1}^{(1)}(\boldsymbol{p}) = \pm\sqrt{3}\pi B\sum_{t_s}\frac{p_\perp}{i\kappa}\frac{\exp[if(t_s)]}{\sqrt{-if''(t_s)}}, \quad (10)$$

where $p_\perp$ and $p_\parallel$, respectively, represent the momentum components perpendicular and parallel to the laser polarization. Finally, the photoelectron momentum distribution is obtained by $w(\boldsymbol{p}) = |M(\boldsymbol{p})|^2$. The energy spectra of photoelectrons can be obtained,

$$\frac{\partial P}{\partial E} = \int w(\boldsymbol{p})2\pi p\sin\theta d\theta, \quad (11)$$

where θ is the emission angle of the photoelectron with respect to the laser polarization.

C. Elastic scattering differential cross sections

As is well known, the standard potential scattering theory for the magnetic quantum number $m = 0$ has been well documented in the text book [44]. For a spherical potential $V(r)$, the scattering-state wave function can be acquired by solving the following stationary Schrödinger equation [44],

$$\left[-\tfrac{1}{2}\nabla^2 + V(r) - \tfrac{1}{2}k^2\right]\varphi_0(\boldsymbol{r};k) = 0, \tag{12}$$

where k is the momentum of the incident electron. For a short-range potential, the scattering wave function satisfies the boundary condition of the asymptotic outgoing wave [44],

$$\varphi_0(\boldsymbol{r};k)|_{r\to\infty} = \frac{1}{(2\pi)^{3/2}}\left[\exp(ikz) + f_0(k,\theta)\frac{\exp(ikr)}{r}\right], \tag{13}$$

where the incident electron wave is chosen as the plane wave along the z axis and θ is the scattering angle. $f_0(k,\theta)$ is the scattering amplitude at a fixed angle and a specific incident momentum. The elastic scattering DCS is then given by $|f_0(k,\theta)|^2$. The details about the calculations of elastic scattering DCS for $m = 0$ can be found in previous work [33]. Most recently, the elastic scattering DCS for $m \neq 0$ was developed by Tolstikhin and Morishita [45]. For $m \neq 0$, Eqs. (12) and (13) are extended to be [45]

$$\left[-\tfrac{1}{2}\nabla^2 + V(\rho,z) - \tfrac{1}{2}k^2\right]\varphi_m(\boldsymbol{r};k) = 0, \tag{14}$$

and

$$\varphi_m(\boldsymbol{r};k)|_{r\to\infty} = \left[(k\rho)^{|m|}\exp(ikz) + f_m(k,\theta)\frac{\exp(ikr)}{r}\right] \times \exp(im\phi). \tag{15}$$

III. NUMERICAL RESULTS AND DISCUSSIONS

A. Dependence of direct electron spectra on the orbital symmetry

In this subsection, we are interested in the effect of orbital symmetry on the direct photoelectron spectra. In this case, we set $M(\boldsymbol{p}) = M^{(1)}(\boldsymbol{p})$ in the SFA model. Firstly, through deriving the Fourier transformation of Eq. (7), we check the effect of the orbital symmetry on the initial electron momentum distributions. Figure 1 shows the initial electron momentum distributions of fluorine anions for $m = 0$ and $m = 1$, respectively. As one can see, for $m = 0$, most electrons are distributed along the polarization direction of the laser field. For $m = 1$, most electrons are symmetrically distributed on both sides of the polarization axis.

Next, we investigate the effect of orbital symmetry on the direct electron spectra in the few-cycle laser field, based on the TDSE and the SP methods. We show the electric field of the laser pulse in Fig. 2(a) and the SP distributions for the fixed electron energy of 3.4 eV in Fig. 2(b). All SPs are numerically solved from the SP equation. Each group of points in Fig. 2(b) depicts the saddle points for the emission angle from 0° to 180° with a step size of 1°. Three dominant saddle points, SP3–SP5, are marked by the numbers 3–5 in Fig. 2(b). Their real parts represent the moments when the electrons are released.

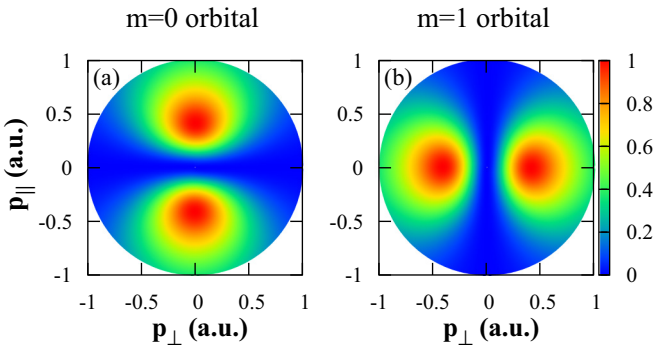

FIG. 1. The two-dimensional (2D) initial electron momentum distributions of fluorine anions for $m = 0$ and $m = 1$, respectively.

In Fig. 3, we show the photoelectron energy spectra in the low-energy region. It can be seen that the energy spectra from the TDSE and the SP method agree well with each other. In addition, there are three striking features in Fig. 3: (i) The electron yield for $m = 1$ is about one order of magnitude weaker than that for $m = 0$; (ii) the main shape of the energy spectra strongly depends on the orbital symmetry; (iii) the location of the dip is independent of the orbital symmetry. The energies corresponding to the first three dips for different orbital symmetries are 0.72, 1.56, and 2.4 eV, respectively.

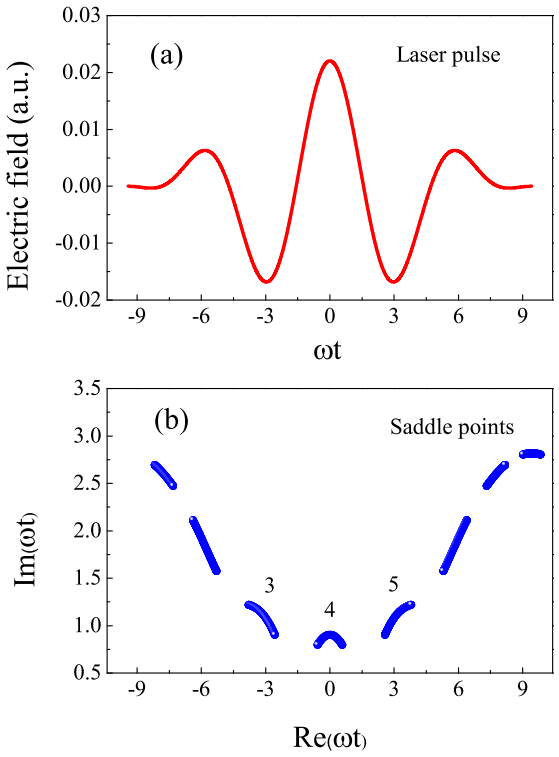

FIG. 2. (a) The electric field of a three-cycle laser pulse with peak intensity of 1.7×10^{13} W/cm^2 and wavelength of 1400 nm. (b) The SP distributions for the fixed photoelectron energy of 3.4 eV in the complex-time plane. The three dominant SPs are marked with numbers.

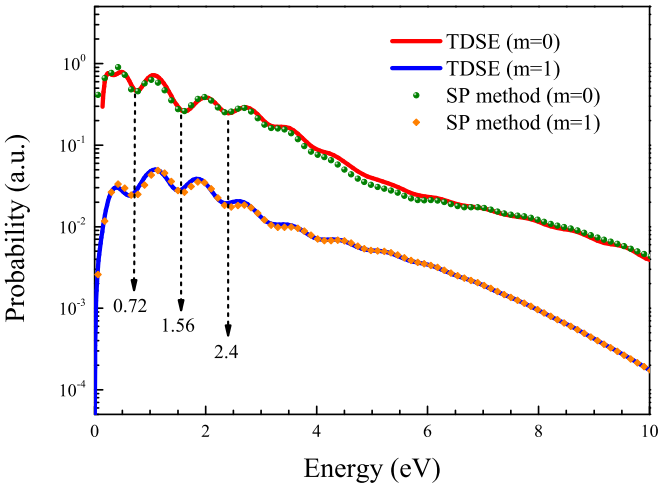

FIG. 3. Angle-integrated energy spectra for fluorine anions by a three-cycle laser pulse with a peak intensity of 1.7×10^{13} W/cm^2 and wavelength of 1400 nm. The energy spectra from the SP method are normalized to the first dip of the TDSE results.

In Fig. 4, the 2D photoelectron momentum distributions (PMDs) in the low-momentum region are displayed. One can clearly see that the results from the SP method are quantitatively consistent with the TDSE results. There is one striking common feature for $m = 0$ and $m = 1$. The interference fringes near the axis $p_\parallel = 0$ are exactly partitioned by three white circles, which is called a "carpetlike structure" in previous work [46]. The three white circles are plotted according to the photoelectron energy of the first three dips in Fig. 3. In addition, two striking differences for $m = 0$ and $m = 1$ can be observed.

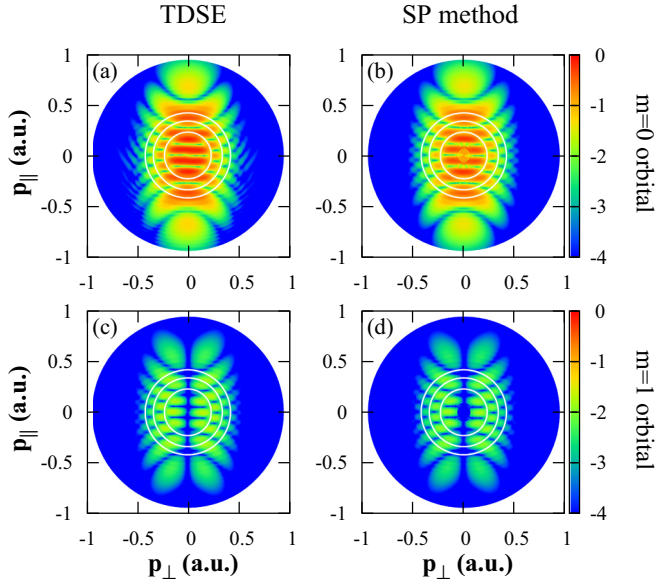

FIG. 4. Photoelectron 2D momentum distributions for fluorine anions by the same laser pulse as in Fig. 3. The three white circles marked in each panel are plotted for the photoelectron energies of 0.72, 1.56, and 2.4 eV, respectively.

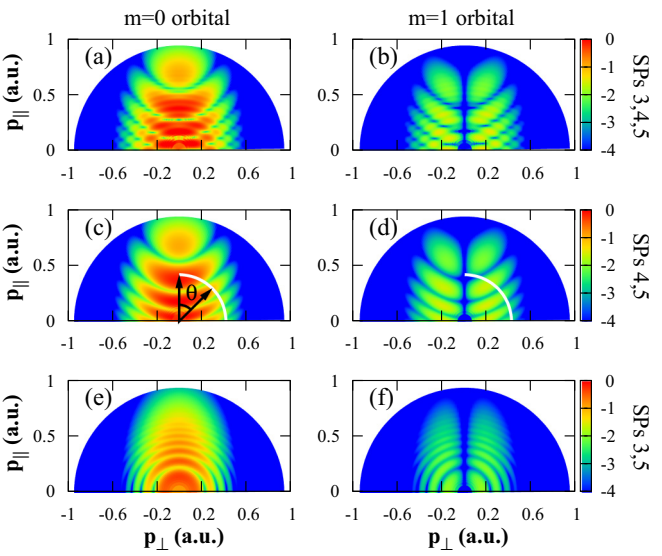

FIG. 5. Photoelectron 2D momentum distributions calculated by considering the saddle points SPs 3–5, SPs 4 and 5, SPs 3 and 5, respectively. The white lines in (c,d) are plotted for the photoelectron energy of 2.4 eV and emission angle θ ranging from 0° to 90°.

First, the PMDs for $m = 1$ are cut by the polarization axis of the laser field. Actually, these particular structures can be directly understood through Eq. (10), which indicates that $M^{(1)}_{\pm 1}(\boldsymbol{p}) \to 0$ when $p_\perp \to 0$. Physically, as seen in Fig. 1(b), there is no electron distributed along the laser polarization axis; therefore no photoelectron signal is expected along this axis.

Second, the number of interference fringes in each white circle for $m = 0$ are different from those for $m = 1$. For example, there are four interference fringes inside the innermost circle of Figs. 4(a) and 4(b) while there are only three on the left-half plane of Figs. 4(c) and 4(d), which tell us that the orbital symmetry also affects the interference patterns.

In order to shed more light on the dependence of the interference patterns on the orbital symmetry, we distinguish the contributions of the dominant SPs on PMDs in Fig. 5. Figures 5(a) and 5(b) show the PMDs by considering coherent superpositions of SPs 3–5. One can see that the main structures of Figs. 4(a) and 4(c) from the TDSE calculations can be well reproduced. Therefore, SPs 3–5 give dominant contributions to the interference patterns in PMDs. In Figs. 5(c)–5(f), we show the PMD by coherently adding the contributions of SP4 + SP5 and SP3 + SP5, respectively. It is clear that the carpetlike structure is absent in these cases. As is well known, intracycle interferences come from the coherent superposition of electron wave packets released in the same optical cycle, whereas the intercycle interferences arise from the coherent superposition of electron wavepackets released in different optical cycles. Therefore, the interference patterns of Figs. 5(c) and 5(d) originate from the intracycle interference from wave packets for SP4 and SP5. The concentric rings centered at zero momentum in Figs. 5(e) and 5(f) are associated with above-threshold detachment (ATD) rings, which originate from the intercycle interference from wave packets for SP3 and SP5. In Fig. 6(a), we plot the projection of the

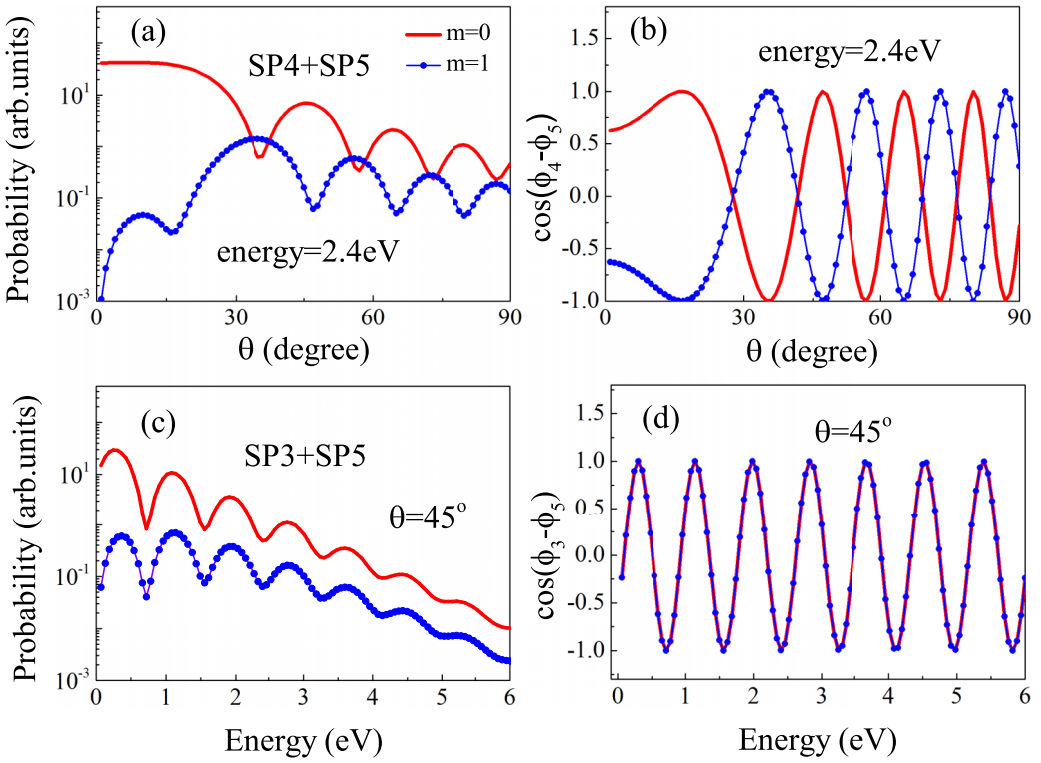

FIG. 6. (a) The projection of the PMDs in Figs. 5(c) and 5(d) along the white lines. (b) The variation of $\cos(\phi_4 - \phi_5)$ with respect to the emission angle for the electron energy at 2.4 eV. (c) The projection of Figs. 5(e) and 5(f) along the emission angle $\theta = 45^\circ$. (d) The variation of $\cos(\phi_3 - \phi_5)$ with respect to the electron energy for the emission angle $\theta = 45^\circ$.

PMDs in Figs. 5(c) and 5(d) along the white lines. Oscillation patterns for $m = 0$ and $m = 1$ are exactly opposite when the emission angles of the photoelectron are larger than 30°.

To facilitate the comprehension of Fig. 6(a), we rewrite the contribution of each SP to the transition amplitude $M^{(1)}(\boldsymbol{p})$ as a complex function $a_n \exp(i\phi_n)$, where a_n and ϕ_n are defined as the amplitude and phase of the nth saddle point, respectively. Figure 6(b) shows the variation of $\cos(\phi_4 - \phi_5)$ with respect to the emission angle for the electron energy at 2.4 eV. $\phi_4 - \phi_5$ is the phase difference of the contributions from SP4 and SP5. We can see that, for $m = 0$ and $m = 1$, the oscillation of $\cos(\phi_4 - \phi_5)$ with respect to the emission angle is exactly opposite when the emission angle changes from 0° to 90°. It suggests that, for the orbitals $m = 0$ and $m = 1$, there is a phase shift of π in the intracycle interference from wave packets for SP4 and SP5.

It is clear that the intracycle interference pattern of different wave packets is dramatically dependent on the orbital symmetry. We also check the effect of orbital symmetry on the intercycle interference pattern. In Fig. 6(c), we plot the projection of Figs. 5(e) and 5(f) along the emission angle $\theta = 45^\circ$. The variation of $\cos(\phi_3 - \phi_5)$ with respect to the energy for the emission angle $\theta = 45^\circ$ is shown in Fig. 6(d). We can see that the intercycle interference pattern from wave packets for SP3 and SP5 is independent of the orbital symmetry. In addition, the energies corresponding to the first three dips in Figs. 6(c) and 6(d) are 0.72, 1.56, and 2.4 eV, respectively, which is consistent with the case of Fig. 3. In fact, we have checked that the above findings are also applicable for other fixed energies or any fixed emission angles. Therefore, it can be concluded that, in the few-cycle linearly polarized laser pulse, the orbital symmetry only affects the intracycle interference pattern, but does not change the intercycle interference pattern much.

B. Dependence of the rescattered electron spectra on orbital symmetry

Now we investigate the effect of the orbital symmetry on the high-energy electron spectra, mainly based on the TDSE and the SFA models. Please note that the following SFA2 results are calculated by numerical integration of Eq. (5). In Fig. 7, we exhibit the photoelectron energy spectra of fluorine anions in a broad range of electron energy for the different orbital symmetry. The yields of photoelectrons for SFA2 and SFA are normalized to the high-energy part of the TDSE results. One can clearly see that, for $m = 1$, the SFA results are in good agreement with the TDSE results. However, for $m = 0$, an appreciable hump structure can be observed between 25 and 30 eV in the TDSE results, which is absent in the SFA results. To reveal the origin of the hump structure in the TDSE results, we also show the results based on the well-established quantitative rescattering (QRS) model [30–33]. The hump structure has been successfully reproduced in the QRS results. According to the QRS model, the momentum distributions of high-energy electrons can be expressed as the product of a returning electron wave packet (RWP) with the elastic differential cross sections [30–33]. For the QRS results, the RWPs are obtained from SFA2, while the elastic differential cross sections are calculated based on the theory introduced in Sec. II C. However, for the SFA results, the differential cross sections are calculated based on the plane-wave Born

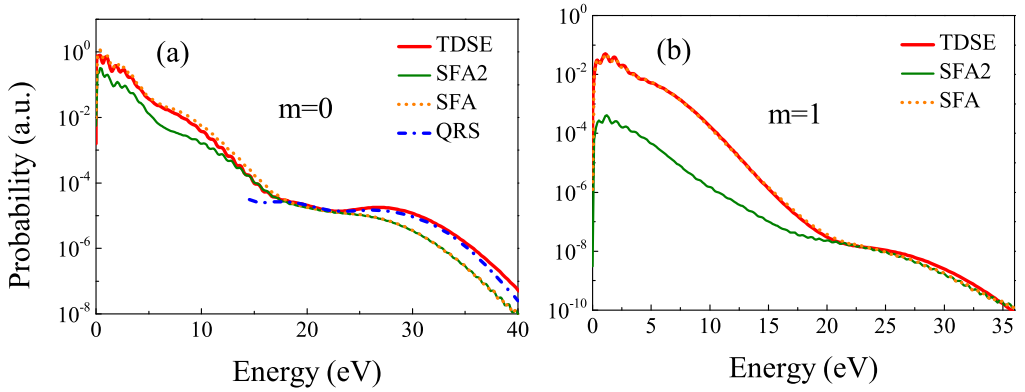

FIG. 7. Angle-integrated energy spectra for fluorine anions in a broad range of electron energy, calculated from the TDSE, the SFA model, and the QRS model. (a) $m = 0$; (b) $m = 1$.

approximation (PWBA) [33]. Therefore, in Fig. 7(a), the difference between the TDSE and SFA results originates from different differential cross sections. The differential cross sections will be discussed in detail in Fig. 9.

Figure 8 shows the whole 2D photoelectron momentum distributions. The results from the TDSE and SFA appear to be quite similar. Here we focus on the outermost ring of the PMDs. The photoelectrons distributing along this ring are called back rescattered ridge (BRR) electrons. The BRR electrons are the electrons that have been rescattered into the backward directions by the residual core. In terms of the classical theory [30–33], the momentum components of the BRR electrons are given by

$$p_{\parallel} = p\cos\theta = \pm A_0 \mp p_r \cos\theta_r, \tag{16a}$$

$$p_{\perp} = p\sin\theta = p_r \sin\theta_r, \tag{16b}$$

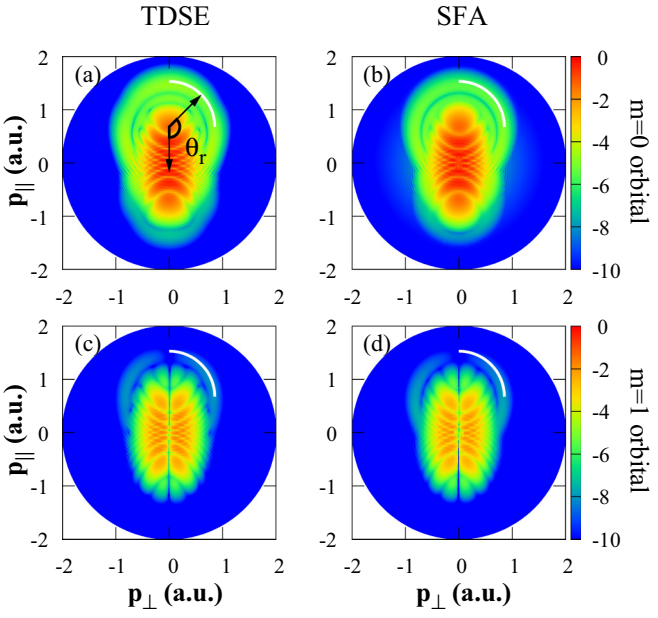

FIG. 8. Photoelectron 2D momentum distributions for fluorine anions in a broad range of electron momentum, calculated from the TDSE and the SFA model. The white line in each panel indicates the location of BRR electrons predicted by Eq. (16); see text for detail.

where the upper signs refer to the case of $p_{\parallel} > 0$ while the lower ones denote the case of $p_{\parallel} < 0$. A_0 is the peak value of the vector potential of the laser pulse. The radius of the BRR ring is $p_r = 1.26A_0$, and the backscattering angle is θ_r, as marked in Fig. 8(a). In Fig. 8, we also plot the BRR ring for θ_r ranging from 90° to 180° with white solid lines in terms of Eq. (16). One can clearly see that the location of BRR rings predicted by Eq. (16) is consistent with those of the TDSE and SFA results. This means that the location of the BRR ring is independent of the orbital symmetry.

In Fig. 9, we show the yields of the photoelectrons along the BRR rings of the TDSE and SFA results. For comparison, we also give the elastic scattering DCS and the DCS from the PWBA method. In Fig. 9(a), the TDSE yield for $m = 0$ shows a clear minimum near $\theta_r = 120°$, which is consistent with the elastic scattering DCS, but the SFA yield on the BRR and the DCS from the PWBA method both decrease monotonically with the increase of the angle. In practice, Eq. (5) of the SFA model is treated by the PWBA method. Thus, the disagreement of the TDSE results and the SFA results is due to the different DCS, and the DCS from the PWBA is not accurate in this case. In Fig. 9(b), it can be seen that SFA yield on the BRR for $m = 1$ monotonically decreases with an increasing angle. By comparing Fig. 9(a) with Fig. 9(b), it is found that the variations of the SFA yield with the scattering angle are similar for the cases of $m = 0$ and $m = 1$, and Eq. (5) of the SFA model is treated by the PWBA method. Thus, the DCS from the PWBA method is independent of the orbital symmetry.

However, the variations of the TDSE yield with the scattering angle are strikingly different for the cases of $m = 0$ and $m = 1$. It can be clearly seen that, when the scattering angle approaches 180°, the TDSE yield for $m = 1$ turns to zero, but the TDSE yield for $m = 0$ increases. This suggests that the elastic scattering DCS for $m = 1$ should be different from those for $m = 0$. Based on the scattering theory for $m \neq 0$ which was recently developed by Tolstikhin and Morishita [45], we also show the elastic scattering DCS for $m = 1$ in Fig. 9(b). It is found that the elastic scattering DCS for $m = 1$ monotonically turns to zero when θ_r is larger than 120°. It indicates that, for the elastic scattering DCS in the case of $m = 1$, the asymptotic behavior toward a larger scattering angle is consistent with that of the TDSE results for

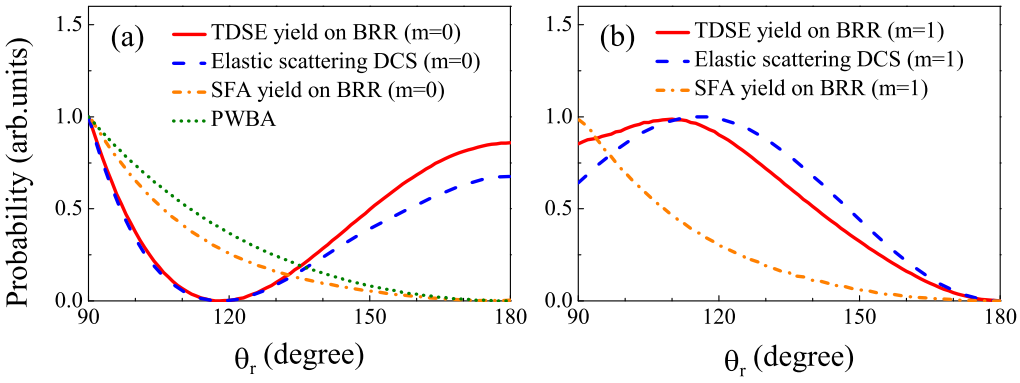

FIG. 9. TDSE yield on the BRR compared with the elastic scattering DCS, and the corresponding results from SFA compared with PWBA. All the data are normalized to unity.

$m = 1$. Therefore, the elastic scattering DCS for $m = 1$ leaves clear fingerprints in the momentum spectra of rescattered photoelectrons for $m = 1$, which is strikingly different from those in the case of $m = 0$.

IV. CONCLUSIONS

In summary, we have carried out a systematic analysis on the photoelectron spectra of fluorine anions in a few-cycle linearly polarized laser pulse, for $m = 0$ and $m = 1$, respectively. The TDSE calculations of the electron spectra for fluorine anions are regarded as the benchmark results. It is found that, for the low-energy electron spectra, although the main shapes of the energy spectra and momentum spectra strongly depend on the orbital symmetry, the locations of dips in the energy spectra and their corresponding rings in the momentum spectra are independent of orbital symmetry. Based on the SP method, further investigations have confirmed that, in a few-cycle linearly polarized laser pulse, the orbital symmetry only affects the intracycle interference pattern, but does not change the intercycle interference pattern. Moreover, based on the QRS theory and the scattering theory developed recently, we find that the elastic scattering DCS leaves different fingerprints in the momentum spectra of rescattered photoelectrons for different atomic orbitals. The present work not only provides a better understanding of the electron dynamics during the direct ionization process of negative ions with valence p orbitals, but also is important for the retrieval of target structure from the momentum spectra of the rescattered photoelectron.

ACKNOWLEDGMENTS

We sincerely thank Prof. Morishita in the University of Electro-Communications in Japan for providing the data for the elastic scattering DCS for $m = 1$. This work is supported by the National Natural Science Foundation of China (Grants No. 11647150, No. 11961131008, No. 11725416, and No. 11664035), the Gansu Provincial Natural Science Foundation of China (Grant No. 18JR3RA230), the Scientific Research Project of Bureau of Gansu Education (Grant No. 2018D-19), and the Foundation of Northwest Normal University (NWNU-LKQN-17-1).

[1] P. B. Corkum, Phys. Today **64**(3), 36 (2011).
[2] F. Krausz and M. Ivanov, Rev. Mod. Phys. **81**, 163 (2009).
[3] D. B. Milošević, G. G. Paulus, D. Bauer, and W. Becker, J. Phys. B **39**, R203 (2006).
[4] W. Becker, X. J. Liu, P. J. Ho, and J. H. Eberly, Rev. Mod. Phys. **84**, 1011 (2012).
[5] X. R. Xiao, M. X. Wang, H. Liang, Q. Gong, and L. Y. Peng, Phys. Rev. Lett. **122**, 053201 (2019).
[6] L.Y. Peng, W. C. Jiang, J. W. Geng, W. H. Xiong, and Q. H. Gong, Phys. Rep. **575**, 1 (2015).
[7] M. V. Frolov, D. V. Knyazeva, N. L. Manakov, A. M. Popov, O. V. Tikhonova, E. A. Volkova, M. H. Xu, L. Y. Peng, L. W. Pi, and A. F. Starace, Phys. Rev. Lett. **108**, 213002 (2012).
[8] Z. Zhang, L. Y. Peng, M. H. Xu, A. F. Starace, T. Morishita, and Q. H. Gong, Phys. Rev. A **84**, 043409 (2011).
[9] M. V. Frolov, N. L. Manakov, and A. F. Starace, Phys. Rev. A **79**, 033406 (2009).
[10] L. Y. Peng, Q. H. Gong, and A. F. Starace, Phys. Rev. A **77**, 065403 (2008).
[11] D. G. Arbó, K. L. Ishikawa, K. Schiessl, E. Persson, and J. Burgdörfer, Phys. Rev. A **81**, 021403(R) (2010).
[12] D. G. Arbó, S. Nagele, X. M. Tong, X. Xie, M. Kitzler, and J. Burgdörfer, Phys. Rev. A **89**, 043414 (2014).
[13] Y. Huismans, A. Rouzée, A. Gijsbertsen, P. S. W. M. Logman, F. Lépine, C. Cauchy, S. Zamith, A. S. Stolodna, J. H. Jungmann, J. M. Bakker, G. Berden, B. Redlich, A. F. G. van der Meer, K. J. Schafer, and M. J. J. Vrakking, Phys. Rev. A **87**, 033413 (2013).
[14] I. Barth and O. Smirnova, Phys. Rev. A **88**, 013401 (2013).
[15] M. M. Liu, Y. Shao, M. Han, P. Ge, Y. Deng, C. Wu, Q. Gong, and Y. Liu, Phys. Rev. Lett. **120**, 043201 (2018).
[16] K. Liu, H. Ni, K. Renziehausen, J.-M. Rost, and I. Barth, Phys. Rev. Lett. **121**, 203201 (2018).
[17] D. B. Milošević, Phys. Rev. A **93**, 051402(R) (2016).
[18] A. Hartung, F. Morales, M. Kunitski, K. Henrichs, A. Laucke, M. Richter, T. Jahnke, A. Kalinin, M. Schöffler, L. Ph. H. Schmidt, M. Ivanov, O. Smirnova, and R. Dörner, Nat. Photonics **10**, 526 (2016).

[19] T. M. Yan, S. V. Popruzhenko, M. J. J. Vrakking, and D. Bauer, Phys. Rev. Lett. **105**, 253002 (2010).
[20] M. Li, J.-W. Geng, H. Liu, Y. Deng, C. Wu, L. Y. Peng, Q. Gong, and Y. Liu, Phys. Rev. Lett. **112**, 113002 (2014).
[21] I. Y. Kiyan and H. Helm, Phys. Rev. Lett. **90**, 183001 (2003).
[22] B. Bergues, Y. Ni, H. Helm, and I. Y. Kiyan, Phys. Rev. Lett. **95**, 263002 (2005).
[23] B. Bergues, Z. Ansari, D. Hanstorp, and I. Y. Kiyan, Phys. Rev. A **75**, 063415 (2007).
[24] B. Bergues and I. Y. Kiyan, Phys. Rev. Lett **100**, 143004 (2008).
[25] A. Gazibegović-Busuladzić, D. B. Milosević, W. Becker, B. Bergues, H. Hultgren, and I. Y. Kiyan, Phys. Rev. Lett. **104**, 103004 (2010).
[26] G. F. Gribakin and M. Y. Kuchiev, Phys. Rev. A **55**, 3760 (1997).
[27] R. Reichle, H. Helm, and I. Y. Kiyan, Phys. Rev. Lett. **87**, 243001 (2001).
[28] J. H. Chen, S. F. Zhao, G. L. Wang, and X. X. Zhou, J. Phys. B: At., Mol. Opt. Phys. **47**, 245601 (2014).
[29] J. H. Chen, M. Han, X. R. Xiao, L. Y. Peng, and Y. Q. Liu, Phys. Rev. A **98**, 033403 (2018).
[30] C. D. Lin, A.-T. Le, Z. Chen, T. Morishita, and R. Lucchese, J. Phys. B **43**, 122001 (2010).
[31] T. Morishita, A.-T. Le, Z. Chen, and C. D. Lin, Phys. Rev. Lett. **100**, 013903 (2008).
[32] M. Okunishi, T. Morishita, G. Prümper, K. Shimada, C. D. Lin, S. Watanabe, and K. Ueda, Phys. Rev. Lett. **100**, 143001 (2008).
[33] Z. Chen, A.-T. Le, T. Morishita, and C. D. Lin, Phys. Rev. A **79**, 033409 (2009).
[34] C. D. Lin, A.-T. Le, C. Jin, and H. Wei, J. Phys. B: At., Mol. Opt. Phys. **51**, 104001 (2018).
[35] V.-H. Hoang, V.-H. Le, C. D. Lin, and A.-T. Le, Phys. Rev. A **95**, 031402(R) (2017).
[36] Z. Chen, Y. Wang, T. Morishita, X. Hao, J. Chen, O. Zatsarinny, and K. Bartschat, Phys. Rev. A **100**, 023405 (2019).
[37] X. X. Zhou, Z. J. Chen, T. Morishita, A.-T. Le, and C. D. Lin, Phys. Rev. A **77**, 053410 (2008).
[38] L. Y. Peng, E. A. Pronin, and A. F. Starace, New J. Phys. **10**, 025030 (2008).
[39] S. N. Song, J. W. Geng, H. B. Jiang, and L. Y. Peng, Phys. Rev. A **89**, 053411 (2014).
[40] D. B. Milošević and W. Becker, Phys. Rev. A **93**, 063418 (2016).
[41] E. Hasović, M. Busuladžić, A. Gazibegović-Busuladžić, D. B. Milošević, and W. Becker, Laser Phys. **17**, 376 (2007).
[42] Z. Chen, T. Morishita, A.-T. Le, and C. D. Lin, Phys. Rev. A **76**, 043402 (2007).
[43] S. F. C. Shearer and M. R. Monteith, Phys. Rev. A **88**, 033415 (2013); G. F. Gribakin and S. M. K. Law, *ibid.* **94**, 057401 (2016).
[44] R. G. Newton, *Scattering Theory of Waves and Particles* (Springer-Verlag, New York, 1982).
[45] O. I. Tolstikhin and T. Morishita, Phys. Rev. A **99**, 063415 (2019).
[46] A. P. Korneev, S. V. Popruzhenko, S. P. Goreslavski, W. Becker, G. G. Paulus, B. Fetić, and D. B. Milošević, New J. Phys. **14**, 055019 (2012).